Unsteady CFD Simulations of Propeller Installation Effects

Arne W. Stuermer*
DLR, German Aerospace Center
Institute of Aerodynamics and Flow Technology
Lilienthalplatz 7, 38108 Braunschweig, Germany

A series of unsteady CFD simulations have been conducted for a set of generic isolated- and installed-propeller configurations at low-speed flight conditions. The propeller geometry investigated is a four-bladed design typical of those used on modern regional turboprop aircraft. The computations were performed with the unstructured DLR TAU-code and the numerical results are compared with experimental data obtained in a wind tunnel test campaign conducted in the 1980s. The results of the unsteady computations performed agree well with the available propeller slipstream data and surface pressure distributions measured in the wind tunnel. Additionally, a detailed analysis and comparison of the forces acting on the wing and the propeller is performed.

Nomenclature

α	Angle of attack, [°]
β_{75}	Blade pitch angle at 75% radius, [°], $\beta_{75} = 29°$
ψ	Azimuth angle, [°]
ψ_{bld}	Blade azimuth position, [°]
ρ	Density, $[kg/m^3]$
b	Wing span, $[m]$, $b = 2.06m$
c	Airfoil chord length, $[m]$, $c = 0.5m$
C_T	Thrust coefficient, [-], $C_T = T/(\rho \cdot n^2 \cdot D^4)$
C_Y	Thrust coefficient, [-], $C_Y = F_y/(\rho \cdot n^2 \cdot D^4)$
C_Z	Thrust coefficient, [-], $C_Z = F_z/(\rho \cdot n^2 \cdot D^4)$
D	Propeller diameter, $[m]$, $D = 0.64m$
J	Advance ratio, [-], $J = V_0/(n \cdot D)$, $J = 0.705$
M	Mach number, [-]
n	Propeller rotational speed, $[1/s]$
q	Dynamic pressure, $[N/m^2]$
q_0	Free stream dynamic pressure, $[N/m^2]$
R	Propeller radius, $[m]$, $R = 0.32m$
r	Radial position, $[m]$
Re	Reynolds number, [-]
T	Propeller thrust, $[N]$
V_0	Free stream velocity, $[m/s]$
x	Axial position, $[m]$

I. Introduction

THE extended capabilities of the unstructured DLR-TAU code to handle Chimera grids in relative motion[1,2,3] have recently enabled the codes application to the simulation of the complex aerodynamics

*Research Aerodynamicist, Transport Aircraft Simulation Branch.

of propeller flows.[4] In a series of unsteady CFD computations focused on the investigation of the complex mutual interaction of propeller slipstream and aircraft components, two generic configurations were investigated:

- An isolated propeller configuration with an axisymmetric nacelle (AGARD 1)
- An installed tractor propeller configuration, with an axisymmetric nacelle mounted mid-way on an untwisted wing with a symmetric airfoil (AGARD 2)

In both cases a four-bladed propeller design typical of modern regional turboprop aircraft is used. These configurations were extensively investigated in a series of wind tunnel tests conducted in the 1980s by FFA, the Aeronautical Research Institute of Sweden, which is now a part of the Swedish Defense Research Agency FOI[5,6] and are also included in an AGARD report on CFD test cases.
The flow parameters set for the CFD simulation correspond to a run in the wind tunnel test at typical low-speed take-off conditions, with an onflow Mach number of $M = 0.15$, a Reynolds number of $Re = 1.7 \cdot 10^6$, angles of attack of $\alpha = 0°$ and $\alpha = 10°$, an advance ratio of $J = 0.705$ and a blade pitch angle of $\beta_{75} = 29°$.

II. Computational Strategy

A. Grid Generation

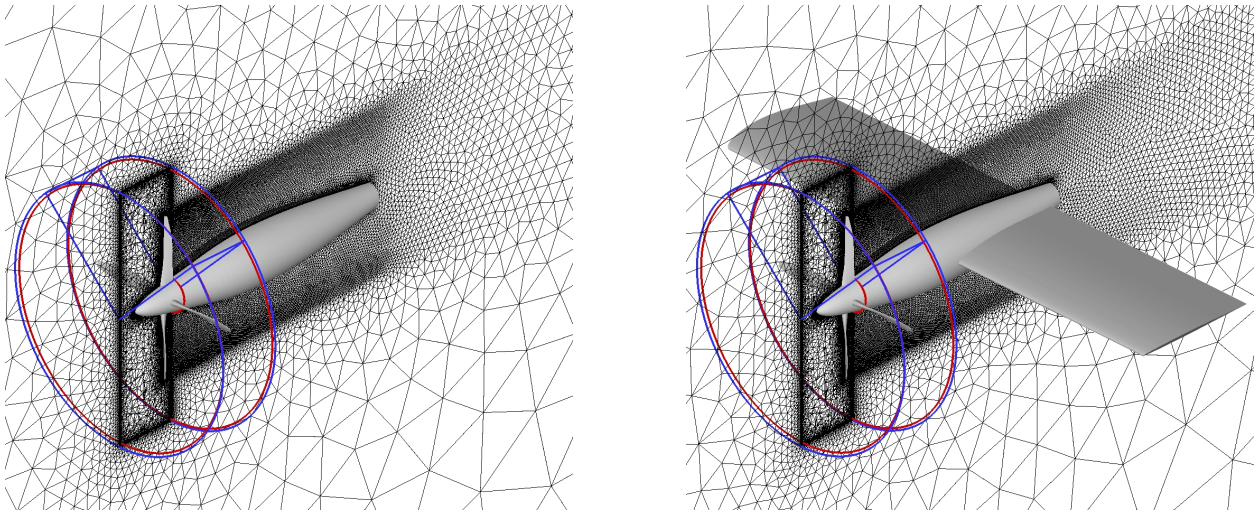

(a) Combined AGARD 1 Chimera grid

(b) Combined AGARD 2 Chimera grid

Figure 1. Two-block unstructured Chimera grids

The unstructured grids shown in figure 1 for the computations are created using the CentaurSoft Centaur grid generation software.[7] This tool has been used extensively at DLR for various unstructured grid based CFD applications. The two-block Chimera grids used for these computations require taking special care during the creation of the CAD geometry for use with the Chimera grid approach as currently implemented in the DLR TAU-code. This approach necessitates leaving a cylindrical hole in the nacelle grid block at the position of the propeller. In addition, an adequate overlap of the two separately generated grids needs to be assured through the appropriate positioning of the geometric boundaries which make up the Chimera boundaries. The first of the two grid blocks was created for the nacelle part of each of the configurations. As the nacelle or the nacelle-wing geometry is symmetric to the Cartesian xz-plane along the centerline, the mesh was generated for half of the domain and subsequently joined with its' mirror image. To ensure an adequate resolution of the propeller wake and the blade tip vortices, very small grid elements were generated in a cylindrical area downstream of the propeller disc. The boundary layers are resolved using 25 layers of prismatic elements.

For the second block a grid was generated around the rotating parts of the geometry, i.e. the spinner, hub and the propeller blades. Again, use was made of the symmetrical nature of the geometry. A 90° slice, i.e. one blade passage, was meshed and subsequently copied and rotated to complete the cylindrical propeller grid block. This strategy guarantees that all four blade passages have an identical spatial discretization greatly enhancing the ability of the CFD solver to resolve the expected periodic fluctuations of the flow. In order to reduce the size of the grids in the present investigations, all surfaces of the propeller are treated as inviscid walls, therefore eliminating the need for prismatic cell layers to resolve boundary layers.
The combined two-block grid for the isolated nacelle configuration in figure 1(a) has 4.980.211 nodes. The joined two-block hybrid Chimera grid for the configuration with the wing, shown in figure 1(b), has a total of 7.273.212 nodes. As in the experiment, the CAD geometry has a small $1mm$-gap between the spinner and nacelle. Care was taken to ensure at least two cells make up this and all of the other Chimera overlap regions in each of the two grid blocks.

B. TAU Computations

The computations performed here were conducted using the DLR TAU-code.[1,8] TAU is an unstructured finite-volume vertex-based CFD solver. It employs an edge-based data structure, also known as a dual-grid approach, which makes the solver very flexible in the types of grid elements it can handle (e.g. tetrahedral, prismatic, pyramidal, and hexahedral elements) and also serves to enhance the memory efficiency of the code. Spatial discretization of the convective fluxes is done using a second order central differencing scheme with scalar or matrix dissipation or through Roe- and AUSM-type upwind schemes. The viscous fluxes are discretized with central differences. Time integration of the governing equations in TAU is alternatively based on an explicit three-stage Runge-Kutta scheme or an implicit LUSGS-scheme and typical state-of-the-art convergence acceleration techniques such as local time stepping, residual smoothing and multigrid are available. Several interfaces for multidisciplinary applications are available. TAU can be efficiently used on scalar as well as on vector computers and on massively parallel machines using MPI based parallelization. Both one- and two-equation turbulence models are implemented for use in viscous simulations.[9,10] Furthermore, the DLR-TAU code offers solution based grid adaptation both through addition as well as the redistribution of grid nodes as required to improve resolution of important aerodynamic flow features.

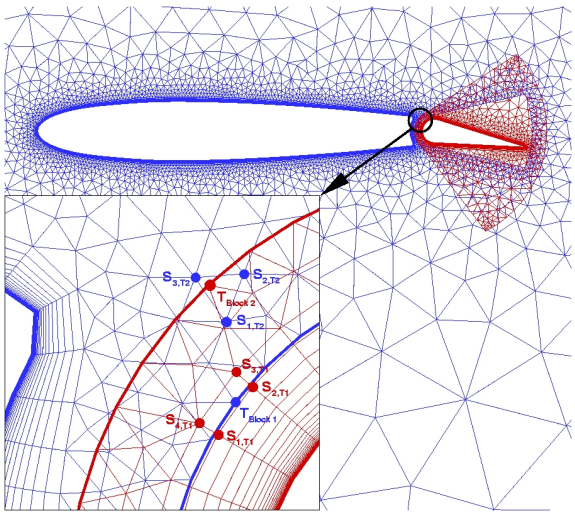

Figure 2. Chimera grid for a wing-flap geometry

The computation of propeller flows present some unique requirements to the CFD method. The solver must be capable of handling multiple rigid bodies in relative motion, since the propeller needs to rotate relative to the stationary nacelle, and it must be possible to compute a time-accurate unsteady solution.
The well-established dual time approach is used in the DLR TAU-code to compute unsteady flows.[11] It is based on a 3-point backward-difference approximation in the physical time. For each discrete physical time step a solution is obtained through a time-stepping procedure in a pseudo-time making use of the same convergence acceleration techniques used for steady-state computations, namely the Runge-Kutta or LUSGS scheme, local time stepping, multigrid and implicit residual smoothing.
Some recent extensions to the DLR TAU-code are the implementation of the Chimera technique and a comprehensive set of motion capabilities. The Chimera approach is based on using several independently generated grids which have regions of overlap.[2,3] An example of a two-block Chimera grid is shown for a simple two dimensional wing-flap geometry in figure 2. During the flow solution process the conservative variables required at a Chimera boundary node of one grid block are interpolated from the node values of the surrounding cell of the other grid block. As an example, for a target node on the Chimera boundary of the flap block, marked as T_{Block2}, the interpolation draws on the source grid nodes $S_{1,T2}$, $S_{2,T2}$ and $S_{3,T2}$ of the wing block. A unique implementation was necessary in the TAU-code, as the solver is based on the dual-grid approach. While this is beneficial for the memory efficiency during the flow simulation, the draw-

back for the Chimera technique is that the flow solver only has information on the edge-node connectivity of the computational grid. As previously described, it is necessary for the Chimera interpolation to retain information on the surrounding nodes of a donor cell, i.e. to have access to some of the primary grid metrics. An extensive set of motion libraries enables arbitrary translational or rotational motion of a grid block. For multi-block cases these libraries allow relative motion between the blocks. For the propeller computations described here, a rotation of a grid associated to the propeller part of the geometry is specified, which requires a recomputation of the Chimera interpolation coefficients after each incremental movement.

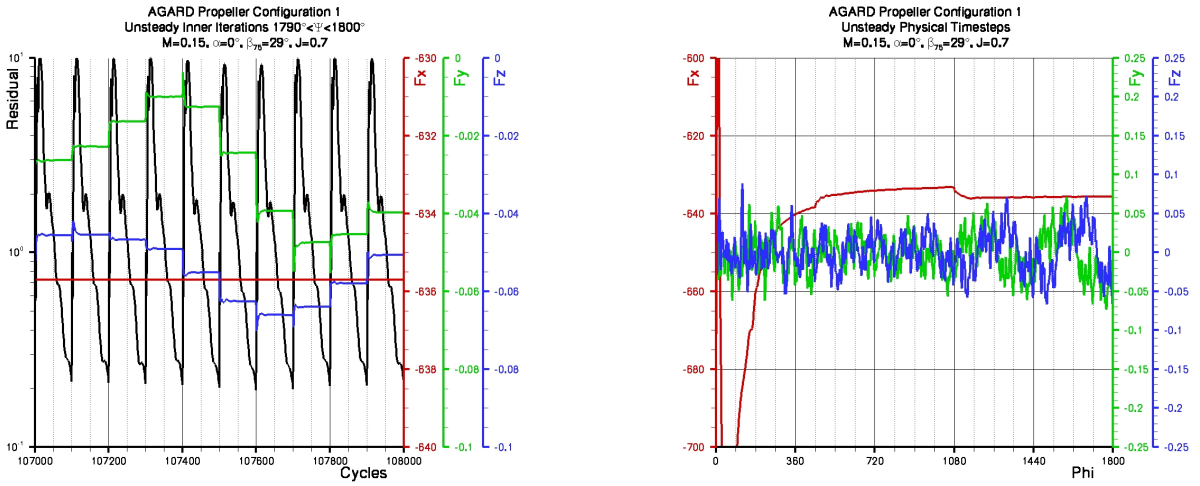

(a) Convergence of the inner iterations

(b) Convergence of the physical time steps

Figure 3. Convergence for the computations of the isolated propeller configuration

The isolated and installed propeller configuration simulations were started from a flow-field initialized with the farfield conditions using the dual time method. One propeller revolution was resolved with 360 dual-time steps with 50 inner iterations each, resulting in a one degree rotation of the propeller block relative to the stationary nacelle block per time step. Convergence of the forces acting on the propeller was attained in each physical time step as can be seen for the example of the isolated propeller computation at $\alpha = 10°$ angle of attack in figure 3(a). To achieve convergence and periodicity in the fluctuations of the propeller forces, five full propeller revolutions were computed to ensure the propeller slipstream is properly developed and has been propagated well over and past the nacelle. The temporal development of the propeller force coefficients during the five revolutions is shown for the example of the isolated propeller computation at $\alpha = 10°$ angle of attack in figure 3(b). All the computations used a central spatial discretization with matrix dissipation, a 3v-multigrid cycle, the 3-stage Runge-Kutta scheme with local time-stepping in the pseudo time of the dual time method and turbulence was modeled using the one-equation Spalart-Allmaras turbulence model as modified by Edwards.[9,10]

III. Results and Validation

A. Propeller Slipstream Development

In order to validate the results of the unsteady computations, the numerically computed propeller wake development is compared with the available experimental data. In this and all the discussions to follow azimuthal positions relative to the axis of propeller rotation are used. These are defined as being $\psi = 0°$ at the top of the nacelle and increase in the direction of propeller rotation, i.e. clockwise when looking at the propeller from behind.

Figure 4 show comparisons of the computed and measured non-dimensionalized dynamic pressure profiles for the installed propeller configuration at a position of $x/R = 0.14$ and $x/R = 1.75$ behind the propeller, marked with the dashed red line in the figure, and along rays extending out at a 45° angle above ($\psi = 45°$) and

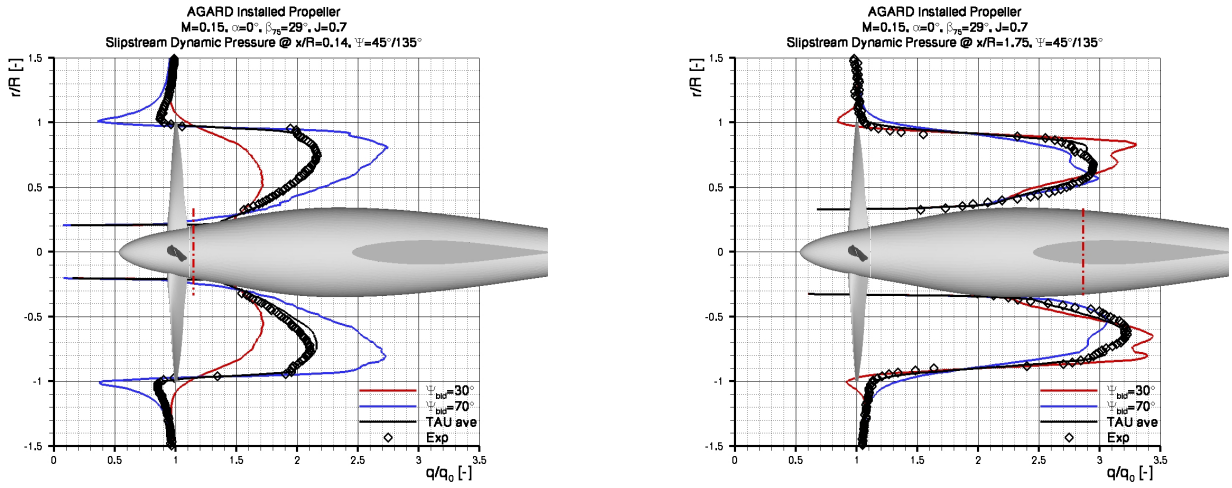

(a) Dynamic pressure profiles @ $x/R = 0.14$

(b) Dynamic pressure profiles @ $x/R = 1.75$

Figure 4. Installed propeller slipstream development

below ($\psi = 135°$) the wing on the right side of the nacelle. In the experiments the slipstream development was measured with a 5-hole probe and thus is in effect time-averaged data. The numerical results allow an analysis of the unsteady fluctuations present in the slipstream, which are periodic for every 90°-rotation of the propeller due to the blade count of four. In each of the figures the CFD results are plotted versus the experimental data both as a time-averaged result, shown as the solid black lines, and as a snapshot at two selected times during a propeller rotation of 90°, shown as the red and blue lines. The time accurate profiles were selected from the computational results to show the extrema of the unsteady fluctuations present in the propeller slipstream.

The time-averaged dynamic pressure profiles at both axial stations, shown as the solid black lines in figures 4(a) and 4(b), are in excellent agreement with the wind tunnel data with both the general profile shape and the magnitudes being correctly predicted in the simulations. A slight deviation is visible at the slipstream boundary in figure 4(b). This difference is most likely attributable to the known inaccuracy of the probe measurements in this region of strong flow gradients. The two selected time-accurate dynamic pressure profiles at the reference blade positions of $\psi_{bld} = 30°$ and $\psi_{bld} = 70°$ clearly show the strong unsteady variations in the magnitude of dynamic pressure during the propellers rotation, in particular for the station immediately aft of the propeller in figure 4(a). These fluctuations are due to the periodic passage of the blade wake. Additionally a pronounced peak and trough develop in the boundary region of the slipstream which is linked to the passage of the blade tip vortex. A clear asymmetry in the propeller slipstream develops as it is propagated over the wing, shown for example in figure 4(b). Larger dynamic pressures occur on the wings lower side. Due to the direction of propeller rotation there is a swirl present in the prop wash, which leads to an acceleration of the flow around the wing leading edge towards the wing lower side on the right side of the nacelle.

B. Propeller-Wing Interaction

The propeller slipstream has a very pronounced impact on the aerodynamics of the wing. This influence is driven by two characteristics of the prop wash: the increased velocities in comparison to the free stream flow and the swirl, or rotation of the prop wash, due to the direction of rotation of the propeller. The swirl of the propeller slipstream leads to a change in the local angle of attack for those wing sections of the installed propeller configuration lying within the prop wash. On the side of the nacelle with an upward rotation of the blades a locally positive angle of attack is the result leading to a positive lift force being produced by the wing, while on the other side of the nacelle the situation is reversed. Additionally, the unsteady nature of the propeller slipstream discussed above leads to a strongly unsteady interaction with the wing. This results

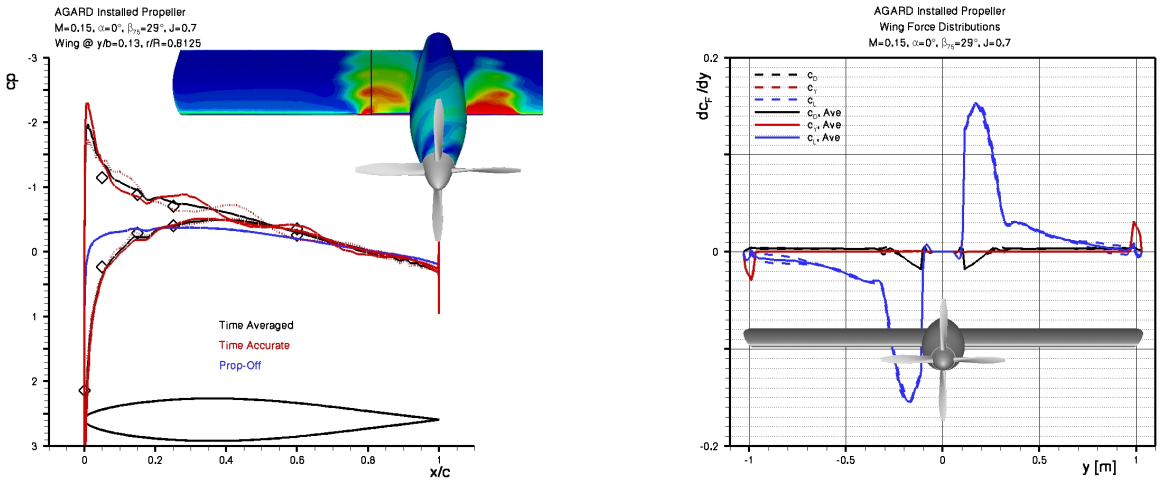

(a) Wing pressure distribution

(b) Spanwise wing force distributions

Figure 5. Impact of the propeller slipstream on the wing

in periodic fluctuations in the pressure distributions, as can be seen in figure 5(a) for a wing section at a spanwise location of $y/b = 0.13$ within the area directly washed over by the propeller slipstream on the side of the nacelle of downward propeller rotation. As for the wake velocities, the four blades of the propeller result in a periodicity of the fluctuations for every 90° of propeller revolution. Two time-accurate pressure distributions from the unsteady CFD results are shown as solid and dotted red lines to show the amplitude of the fluctuations while a time-averaged pressure distribution is shown as a solid black line to allow a better comparison with the experimentally measured data. To help illustrate the impact of the propeller slipstream on the wing, figure 5(a) also includes a blue line, which shows the wing pressure distributions for the same airfoil section taken from a computation of the configuration without propeller. Due to the symmetric airfoil sections the pressure distribution in the latter case is identical both on the upper and lower wing surface.
The airfoil section shown in figure 5(a) lies towards the outer boundary of the prop wash at a radial position of $r/R = 0.8125$, and thus exhibits a strong impact of the periodic passage of the blade tip vortex. This can be seen in the amplitudes of the fluctuations in the two time-accurate pressure distributions both in the suction peak levels and in chordwise direction. The high velocities in the propeller slipstream lead to the development of a more pronounced suction peak at the leading edge than is seen for the airfoil pressure distribution of the unpowered configuration. The agreement between the time-averaged CFD results and the experimental data is good with the most noticeable differences limited to the suction peak levels which tend to be over predicted slightly in the computations.
Figure 5(b) shows the spanwise force distribution of the wing. Again a time-averaged value and two time-accurate results from the unsteady CFD simulation are shown as solid and dashed lines respectively, with the black lines showing the drag distribution, the red lines the side-force and the blue lines the lift. The slipstream swirls effect on the local angle of attack of the wing sections lying within the prop wash leads to large lift forces being produced in this region. As the wing consists of a symmetric airfoil with no twist a positive lift is produced on the left side of the nacelle where the propeller blades rotate upwards while on the opposite side a negative lift of equal magnitude is produced. In addition to the direct local impact of the prop wash, a spanwise influence is also visible with the lift distribution gradually dropping off towards the tips. The unsteady nature of the propeller slipstream leads to a slight oscillation of the maximum lift forces acting on the wing in the prop wash and in particular to a fluctuation in the spanwise lift distribution towards the tip of the wing.
The drag distribution shows negative drag acting on the wing in the area affected by the prop wash. This is the result of the pronounced suction peaks seen on the wing leading edge in figure 5(a) in this region, which result in a localized thrust contribution of the wing.

C. Propeller Forces

Figure 6 shows the development of the thrust, lateral and lift force coefficients produced by a blade during one full propeller revolution as evaluated from the computational results using the post-processing tool AeroForce.[12] The forces are plotted as a comparison between the CFD results for the isolated propeller configuration, shown as solid lines, and the installed configuration as dashed lines, both at an angle of attack of $\alpha = 0°$.

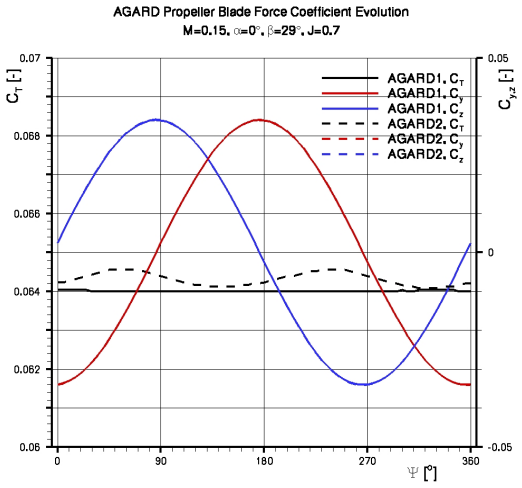

Figure 6. Blade force coefficients development during rotation

For the isolated propeller configuration the blade produces a constant thrust force for the entire propeller revolution, shown as the solid black line, as the relative flow for each blade section, the vector sum of the rotational and the onflow velocity component, is constant for this axial flow case. The blade thrust production of the installed configuration, the dashed black line, exhibits a sinusoidal oscillation with two force cycles per propeller revolution. This force fluctuation can be attributed to the mutual interaction between the wing and the propeller, which leads to the blade being affected by an altered flowfield as it passes in front of the wing on its downward and upward rotation. This interaction with the wing causes a small increase in the overall blade thrust force for this configuration over the isolated propeller case.

The lateral force coefficient, shown in red, exhibits a one-cycle sinusoidal oscillation during the blades rotation around a mean value of zero, as the evaluation of the forces is performed in a stationary frame of reference fixed to the nacelle. The maxima occur at positions of $\psi_{bld} = 0°$ and $\psi_{bld} = 180°$, i.e. when the blade is at the top or the bottom of its rotation. These are the positions at which the blade force vector has the largest component pointing in the direction of the y-axis.

The evolution of the lift force coefficient, shown in blue, exhibits an identical one cycle sinusoidal fluctuation, but shifted up to earlier blade azimuthal positions by 90°. These positions, to the left and right of the nacelle, have the largest contributions of the blade force vector pointing in the direction of the z-axis, i.e. the top and the bottom of the nacelle. Both of these in-plane forces show no visible impact of the presence of the wing.

An increase in the angle of attack has a noticeable impact on the blade and therefore on the overall propeller force coefficients. This is due to a component of the freestream velocity being aligned with the plane of propeller rotation, as shown in figure 7(a). For each blade this component is both dependant on the angle of attack of the propeller and the azimuthal position of the blade, leading to a variable local incidence angle and relative velocity for a blade as it rotates. This effect is most pronounced when comparing the local flow conditions for an airfoil section of a downmoving blade on one side of a propeller at a positive angle of attack to those of the upmoving blade on the other side. As can be seen in figure 7(a), the relative velocity is larger and at a greater local incidence angle for the downmoving blade airfoil than it is for the upmoving section. This naturally results in larger forces being produced on the downmoving blades than on the upmoving blades. Figure 7(b) compares the blade thrust, lateral and lift force coefficients during one rotation for the isolated propeller at $\alpha = 0°$ and $\alpha = 10°$ angle of attack. The solid black line shows that the blade thrust coefficient at angle of attack exhibits a one-period sinusoidal oscillation, with a thrust maximum at a blade position of $\Psi = 100°$, during the blades downward rotation, and the minimum at $\Psi = 280°$, during the blades upward sweep.

The blade lift at $\alpha = 10°$, the solid blue line in figure 7(b), shows a comparable sinusoidal development during the rotation as it does at $\alpha = 0°$, but the maximum lift coefficient value at $\Psi = 85°$ is increased due to the larger relative velocities and local angles of attack during this part of the rotation, while the minimum value at $\Psi = 265°$ is reduced.

The blade lateral force at $\alpha = 10°$, shown as the solid red line in figure 7(b), shows a deviation from the perfectly sinusoidal oscillation seen at $\alpha = 0°$. The magnitude of the minima is slightly reduced, but occurs at a slightly later blade azimuthal position. The maximum lateral force during the latter part of the down-

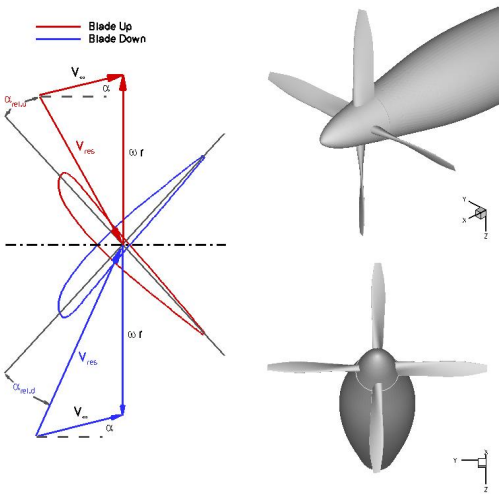

(a) Asymmetric flow for propeller at angle of attack

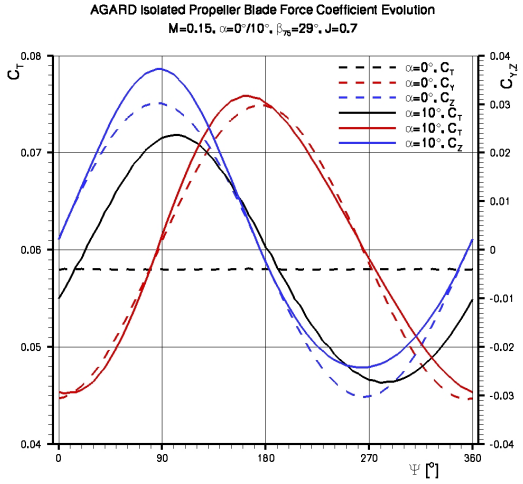

(b) Comparison of blade forces at $\alpha = 0°$ and $\alpha = 10°$

Figure 7. Impact of propeller AoA on blade forces

ward sweep is shifted to an earlier azimuthal position, occurring at $\Psi = 160°$ versus $\Psi = 175°$ at $\alpha = 0°$ and shows a slight increase in magnitude.

Table 1 lists the propeller coefficients for the various cases as measured in the wind tunnel in comparison with the CFD results. The range given for the experimental values represent the minimum and maximum values taken from several runs at an advance ratio of $J = 0.705$ used in the CFD simulations, while the value in parentheses are the median of these values.

The computation of the isolated propeller configuration over predicts the average value of the experimental propeller thrust coefficient by 5.5%. Initial results from a computation in which a Navier-Stokes grid was also used for the propeller block results in a thrust coefficient that falls within the range of values found in the wind tunnel tests and is 6% lower than the value from the computation in which the blades were modeled as inviscid walls.

Both the experimentally and the numerically determined thrust coefficients indicate that the presence of the wing in the propeller slipstream leads to a small increase in propeller thrust. As discussed for the blade thrust force coefficient, this is due to the mutual interaction of the propeller slipstream and the wing, in which the latter acts as a stator and dimishes the swirl in the prop wash. For this geometry the computations over predict the average thrust coefficient found in the experiments by 4.7%, which is in line with the tendency seen for the isolated propeller configuration. Therefore it can be assumed that modeling the blades as viscous walls in a computation should also lead to an excellent agreement with the wind tunnel data.

	C_T	C_Y	C_Z
Isolated Propeller			
Experiment, $\alpha = 0°$	0.236 - 0.248 (0.2435)	-	-
TAU, $\alpha = 0°$	0.25695	0	0
TAU, $\alpha = 10°$	0.2614	0.00437	0.0175
Installed Propeller			
Experiment, $\alpha = 0°$	0.233 - 0.260 (0.2465)	-	-
TAU, $\alpha = 0°$	0.2581	0	0

Table 1. Propeller force coefficients

The table also reflects the impact of the propeller angle of attack on the propeller forces. While both lift and lateral force coefficients of the isolated propeller at $\alpha = 0°$ are zero, they increase to values of $C_Z = 0.0175$ and $C_Y = 0.00437$, or 7% or 2% of the thrust respectively at $\alpha = 10°$.

The increase in the propeller lift forces is easily understood by looking at a pair of diametrically opposed blades. At positive incidence angles, a lift force is produced on a downmoving blade, which benefits from the increased relative velocities and incidence angles due to the propeller angle of attack (see figure 7(a)), while the diametrically opposed upmoving blade generates lower forces in the opposite direction due to the lower relative velocities and incidence angles, as shown in figure 7(b). The latter cannot fully compensate for the forces generated on the opposing side of the propeller, resulting in a net lift force being produced. For a set of diametrically opposed blades of this propeller, a two-period sinusoidal net lift evolution during the rotation results, which is shown as the black bars in figure 8(a). As the resulting lift force for the remaining blade pair is identical to this but merely shifted by 90°, the total net lift force for the propeller blades is a constant value.

The generation of the propeller lateral force is not as easily understood as is the total lift force production at incidence, since figure 7(b) shows the blade lateral force component changing its sign on both the upmoving and downmoving side of the propeller. Figure 8(b) shows the resulting lateral force of two diametrically opposed blades for the propeller at $\alpha = 10°$ angle of attack. As described earlier, the blade lateral force coefficient does not exhibit a perfectly sinusoidal evolution during the rotation. This means that net positive lateral forces of two diametrically opposed blades, shown as the black bars in the figure, are produced for a slightly larger portion of the revolution, and these are also slightly greater in their peak magnitude compared to the negative lateral forces, shown as the gray bars. The constant total propeller lateral force is the result of simply adding to this the resulting lateral force distributions of the next set of opposing blades, which are naturally shifted by 90° to later azimuth angles.

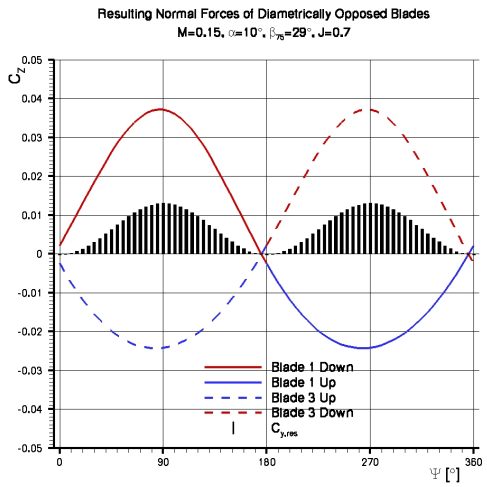

(a) Lift forces for a diametrically opposed blade pair

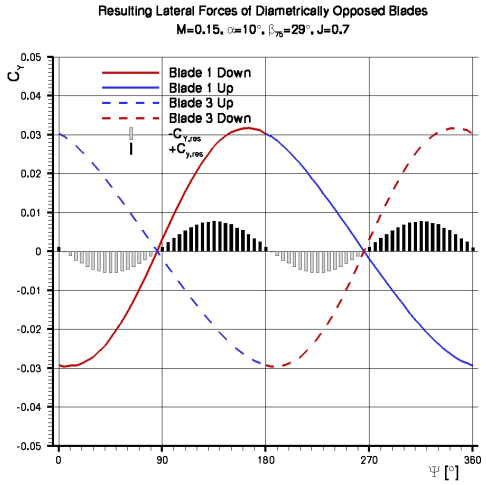

(b) Lateral forces for a diametrically opposed blade pair

Figure 8. Impact of propeller AoA on in-plane propeller forces

D. Power Effects

Figure 9 compares the breakdown of the drag acting on the wing and nacelle of the installed propeller configuration at $\alpha = 0°$, both with and without running propeller, thus allowing an analysis of the power/slipstream impact. The wing drag for the powered configuration, the blue solid line in figure 9(a), shows a four-cycle sinusoidal oscillation with an amplitude of 6 counts during one propeller rotation. This is related to the passage of the four propeller blades in front of the wing, which cause a periodic unsteady fluctuation in the slipstream flow to be propagated across the wing (see figure 4(b)). The mean wing drag of 26 counts for the

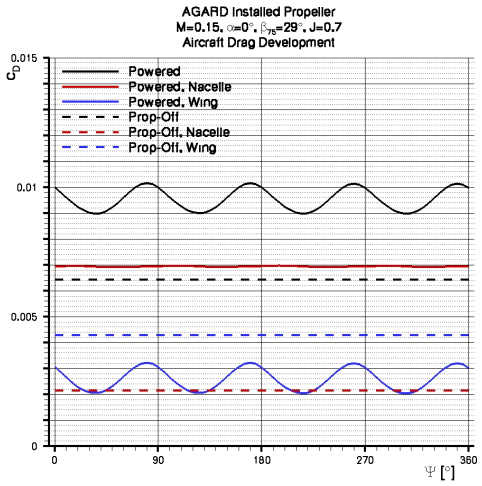

(a) Aircraft component drag

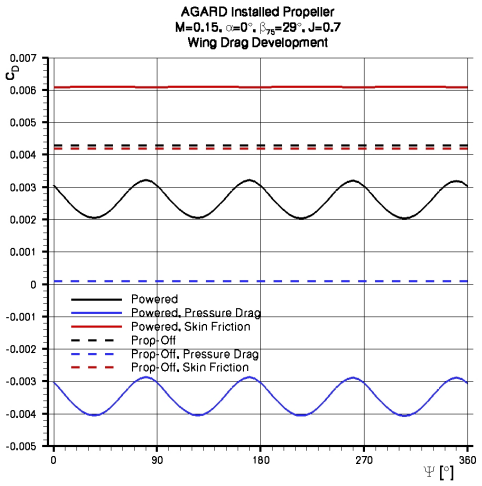

(b) Wing drag breakdown

Figure 9. Propeller Slipstream/Power effect on aircraft drag

powered configuration is much lower than for the unpowered configuration at 43 counts. Figure 9(b) shows that it is the pressure component of the drag, shown as the solid versus the dashed blue line for the powered and unpowered configuration respectively, that are the root cause for this drag difference. The increased velocities in the propeller slipstream were shown to lead to pronounced suction peaks at the leading edge of the wing (figure 5(a)). These result in a net pressure force component in the direction of flight for the powered configuration versus a slight pressure drag for the unpowered case. This drag advantage is not negated by the increase in wing skin friction component under powered conditions, as can be seen in the solid versus the dashed red lines in figure 9(b). However, the propeller slipstream interaction with the nacelle leads to a nacelle drag increase of 48 counts under propeller power. Therefore the overall drag of the powered configuration is increased to a mean value of 95 counts with a fluctuation amplitude of 6 counts versus a value of 64 counts for the unpowered aircraft.

IV. Conclusion

The DLR TAU-code has been applied to the unsteady simulation of generic isolated and installed propeller configurations. A comparison with propeller slipstream data obtained in a series of wind tunnel tests has been performed and the numerical results show good agreement with the experimental data. Furthermore the numerical results showed the very pronounced unsteady effects present in the slipstream, such as the periodic passage of blade tip vortices and blade wakes. The current computations using an inviscid modeling of the propeller blades over predict the propeller thrust coefficient found in the experiments by around 5%. Initial studies employing a no-slip wall boundary condition on the propeller blades indicate that this slightly large computed propeller thrust is attributable to the neglect of skin friction acting on the propeller. An increase of the propeller angle of attack was shown to have a pronounced effect on the in-plane forces, i.e. the lift and lateral forces produced by the propeller. A computation at $\alpha = 10°$ showed that the lift force reaches a level of 7% and the lateral force around 2% of the propeller thrust.
An analysis of the complex mutual aerodynamic interactions between the propeller and the wing has been presented for a generic wing mounted tractor propeller configuration. Both an unsteady fluctuation in the propeller blade thrust force due to the wing as well as the effect of the propeller slipstream on the wings lift distribution has been discussed. A small increase in propeller thrust has been shown to result from these interactions versus the isolated propeller configuration. The slipstream interaction with the wing and nacelle was shown to lead to an overall increase in aircraft drag, despite a thrust contribution resulting from the strong suction peaks at the wing leading edges in the region washed over by the propeller wake.

References

[1]Gerhold, T. and Evans, J., "Efficient Computation of 3D-Flows for Complex Configurations with the DLR-*Tau* Code using Automatic Adaptation," *Notes on Numerical Fluid Mechanics*, edited by W. Nitsche, Vol. 72, Vieweg, Braunschweig, 1998, pp. 178–185.

[2]Madrane, A., Heinrich, R., and Gerhold, T., "Implementation of the Chimera Method in the Unstructured Hybrid DLR Finite Volume TAU-Code," *6th Overset Composite Grid and Solution Technology Symposium*, Ft. Walton Beach, FL, USA, 2002, pp. 524–534.

[3]Madrane, A., Raichle, A., and Stuermer, A., "Parallel Implementation of a Dynamic Unstructured Chimera Method in the DLR Finite Volume TAU-Code," *12th Annual Conference of the CFD Society of Canada*, Ottawa, Ontario, Canada, 2004, pp. 524–534.

[4]Stuermer, A., "Validation of an Unstructured Chimera Grid Approach for the Simulation of Propeller Flows," Tech. Rep. AIAA 2004-5289, 2004.

[5]Samuelsson, I., "Low Speed Wind Tunnel Investigation of Propeller Slipstream Aerodynamic Effects on Different Nacelle/Wing Combinations Part 1," Tech. Rep. FFA TN 1987-22, FFA, 1987.

[6]Samuelsson, I., "Low Speed Wind Tunnel Investigation of Propeller Slipstream Aerodynamic Effects on Different Nacelle/Wing Combinations Part 2," Tech. Rep. FFA TN 1990-24, FFA, 1990.

[7]CentaurSoft, "http://www.centaursoft.com," web page, 2005.

[8]Galle, M., Gerhold, T., and Evans, J., "Technical Documentation of the DLR Tau-Code," Tech. Rep. DLR-IB 223-97/A43, 1997.

[9]Spalart, P. and Allmaras, S., "A One-Equation Turbulence Model for Aerodynamic Flows," Tech. Rep. AIAA 92-0439, 1992.

[10]Edwards, J. and Chandra, S., "Comparison of Eddy-Viscosity-Transport Turbulence Models fot Three-Dimensional, Shock-Separated Flows," *AIAA Journal*, Vol. 34, No. 4, 1996, pp. 756–763.

[11]Jameson, A., "Time Dependent Calculations Using Multigrid, with Applications to Unsteady Flows Past Airfoils and Wings," *10th Computational Fluid Dynamics Conference*, Honolulu, HI, USA, 1991.

[12]Wild, J., "AeroForce: Thrust/Drag Bookkeeping and Aerodynamic Force Breakdown over Components," Tech. Rep. AIRDATA WP4.1, DLR, 1999.